



## Design of Pt/t-ZrO<sub>2</sub>/g-C<sub>3</sub>N<sub>4</sub> efficient photocatalyst for the hydrogen evolution reaction

Huanhuan Li<sup>a</sup>, Yong Wu<sup>a</sup>, Can Li<sup>a,\*</sup>, Yinyan Gong<sup>a</sup>, Lengyuan Niu<sup>a</sup>, Xinjuan Liu<sup>a</sup>, Qing Jiang<sup>b</sup>, Changqing Sun<sup>c</sup>, Shiqing Xu<sup>a,\*</sup>

<sup>a</sup> College of Materials Science and Engineering, China Jiliang University, Hangzhou, 310018, China

<sup>b</sup> School of Materials Science and Engineering, Jilin University, Changchun, 130031, China

<sup>c</sup> School of Electrical and Electronic Engineering, Nanyang Technological University, 639798, Singapore



### ARTICLE INFO

#### Keywords:

Catalyst design  
Work function  
Electron redistribution  
Reaction energy barrier  
Hydrogen evolution reaction

### ABSTRACT

Photocatalytic efficiency of graphitic carbon nitride (g-C<sub>3</sub>N<sub>4</sub>) has been hindered by fast carrier recombination and high reaction energy barriers, which can be improved by combining a semiconductor with a large work function. Based on this strategy, we synthesized a novel Pt/t-ZrO<sub>2</sub>/g-C<sub>3</sub>N<sub>4</sub> composite by integrating g-C<sub>3</sub>N<sub>4</sub> with tetragonal ZrO<sub>2</sub> and Pt nanoparticles. Results of experimental measurements and density functional theory simulation demonstrate that the carrier lifetime, transferability and energy barriers of catalysts depend on their work function. The optimal composite exhibits an extraordinary catalytic ability for hydrogen generation of 722.5  $\mu\text{mol}(\text{gh})^{-1}$  and solar-to-hydrogen energy conversion efficiency of 0.215% under visible-light irradiation, and high catalytic stability. The modification strategy could be applied to designing various different high-efficient catalysts by selecting semiconductors with suitable work functions.

### 1. Introduction

Solar-to-hydrogen (H<sub>2</sub>) conversion, as an effective and sustainable technique, has been widely studied to resolve the global energy and environmental crisis [1–3]. Since the photoelectrochemical water splitting was firstly reported by Fujishima and Honda [4], various photocatalysts have been widely investigated, such as metallic chalcogenides [5–8], phosphides [9], nitrides [10,11], carbides [12,13], and organic semiconductors [14,15]. Among these alternatives, graphitic carbon nitride (g-C<sub>3</sub>N<sub>4</sub>), as a two-dimensional layered materials, possesses the narrow forbidden gap and suitable redox potentials, which is regarded as a potential photocatalyst. Unfortunately, the lifetime of charge carriers is short in the photocatalytic reaction process, limiting its photocatalytic efficiency [16]. To solve this problem, various strategies, such as heterojunction [17–20], artificial defects (vacancy, dopant, etc.) [21,22], and surface modification [23,24], have been developed to enhance the photocatalytic efficiency.

Constructor heterojunction is a simple and effective method, since the characteristic band structure of heterojunction is advantageous for enhancing the charge carrier separation efficiency, thus leading to the improvement of catalytic performances [17,25–27]. Heterojunctions photocatalysts, such as CdTe/TiO<sub>2</sub> [18], CuO/ZrO<sub>2</sub> [28], CaIn<sub>2</sub>S<sub>4</sub>/g-

C<sub>3</sub>N<sub>4</sub> [29], are reported to show the enhanced photocatalytic efficiency. Constructor heterojunction based on g-C<sub>3</sub>N<sub>4</sub> can lengthen the photo-generated charge carrier lifetime due to the electron transfer between them and enhance the photocatalytic performances [23,30–33]. Meanwhile, metal Pt has been usually loaded on substrates and regarded as the reaction active sites of hydrogen evolution reaction (HER), which attributes to the reduction of the energy barrier due to its large work function [1,34]. However, the hydrogen production efficiency of most Pt substrates are still unsatisfactory under visible-light irradiation, since the semiconductor co-catalysts (such as: TiO<sub>2</sub> [35], CoO [36] and LaFeO<sub>3</sub> [37]) with the small work functions reduce the work function of composite catalysts and thus increase the energy barriers of the HER. On account of the large work function, ZrO<sub>2</sub> phase has been regarded as a nice semiconductor co-catalysts to reduce the reaction energy barrier and thus improve the photocatalytic performances of the collaborators [28,38,39]. Considering the large work function difference between ZrO<sub>2</sub> and Pt/g-C<sub>3</sub>N<sub>4</sub>, the energy barrier of the HER on Pt/g-C<sub>3</sub>N<sub>4</sub> may be reduced after combining the ZrO<sub>2</sub> phase. The relevant studies at the electronic and energetic levels are still lack and necessary to be developed to reveal the essence of high photocatalytic efficiency and design new high-efficiency photocatalysts in further.

\* Corresponding authors.

E-mail addresses: [canli1983@gmail.com](mailto:canli1983@gmail.com) (C. Li), [sxucjlu@163.com](mailto:sxucjlu@163.com) (S. Xu).

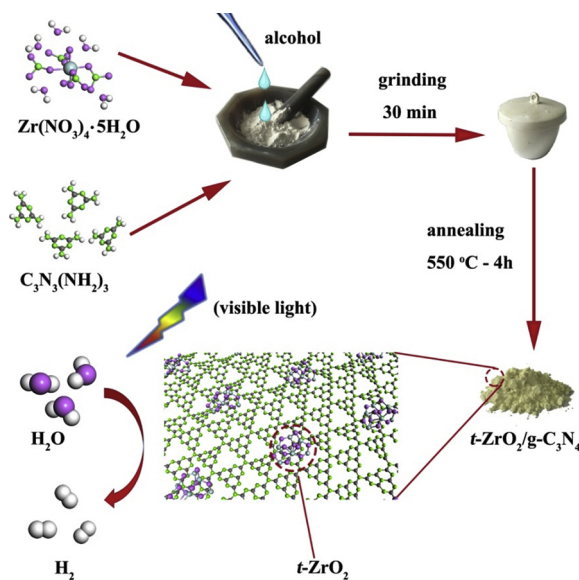


Fig. 1. Schematic illustration for the synthetic route of the  $t\text{-ZrO}_2/\text{g-C}_3\text{N}_4$  composite.

For this purpose,  $t\text{-ZrO}_2/\text{g-C}_3\text{N}_4$  has been designed by supporting the tetragonal  $\text{ZrO}_2$  ( $t\text{-ZrO}_2$ ) nanoparticles on the  $\text{g-C}_3\text{N}_4$  film, and then Pt nanoparticles are loaded to form  $\text{Pt}/t\text{-ZrO}_2/\text{g-C}_3\text{N}_4$  composite photocatalyst. By virtue of the work function regulation and electron redistribution, the  $\text{Pt}/t\text{-ZrO}_2/\text{g-C}_3\text{N}_4$  composite exhibits quadruples

photocatalytic efficiency in comparison to  $\text{Pt}/\text{g-C}_3\text{N}_4$  sample for water splitting of hydrogen generation under visible-light irradiation.

## 2. Results

A series of  $t\text{-ZrO}_2/\text{g-C}_3\text{N}_4$  composite materials were synthesized through a simple one-pot calcination method, as schematically illustrated in Fig. 1 (see the Supporting Information for preparation details). For comparisons, pristine  $t\text{-ZrO}_2$  and  $\text{g-C}_3\text{N}_4$  samples and  $t\text{-ZrO}_2/\text{g-C}_3\text{N}_4$  composite samples with different molar ratios of  $t\text{-ZrO}_2$  and  $\text{g-C}_3\text{N}_4$  were also fabricated.

The microstructure and morphology characterizations of pristine  $\text{g-C}_3\text{N}_4$  and  $t\text{-ZrO}_2/\text{g-C}_3\text{N}_4$  composites are presented in Fig. 2. Fig. 2a shows the XRD pattern of all samples. The two diffraction peaks at around  $13.0^\circ$  and  $27.4^\circ$  indicate the (100) and (002) crystal planes of  $\text{g-C}_3\text{N}_4$  phase with the layered and 3-s-triazine structures, respectively [40,41], which also appear in the composite samples of CN-Z25, CN-Z30, CN-Z33, CN-Z35 and CN-Z40, implying that the  $\text{g-C}_3\text{N}_4$  is present in all composite samples. Meanwhile, the other diffraction peaks of composite samples are consistent with that of  $t\text{-ZrO}_2$  phase (JCPDS 50-1089). Thus, all composite samples consist of the  $\text{g-C}_3\text{N}_4$  and  $t\text{-ZrO}_2$  phases. Moreover, the pristine  $\text{g-C}_3\text{N}_4$  sample shows the bulky morphology with stacking films in SEM image of Fig. 2b, and the composite sample (CN-Z33 as an example) shows the aggregate  $t\text{-ZrO}_2$  nanoparticles (with size of 100 nm in red line segment area) and  $\text{g-C}_3\text{N}_4$  films (blue line segment area) in Fig. 2c. Meanwhile, the TEM images of pristine  $\text{g-C}_3\text{N}_4$  and CN-Z33 samples are displayed in Fig. 2d and e. The smooth and ultrathin  $\text{g-C}_3\text{N}_4$  film has an edge length around 700 nm, and the CN-Z33 sample has the  $t\text{-ZrO}_2$  nanoparticles

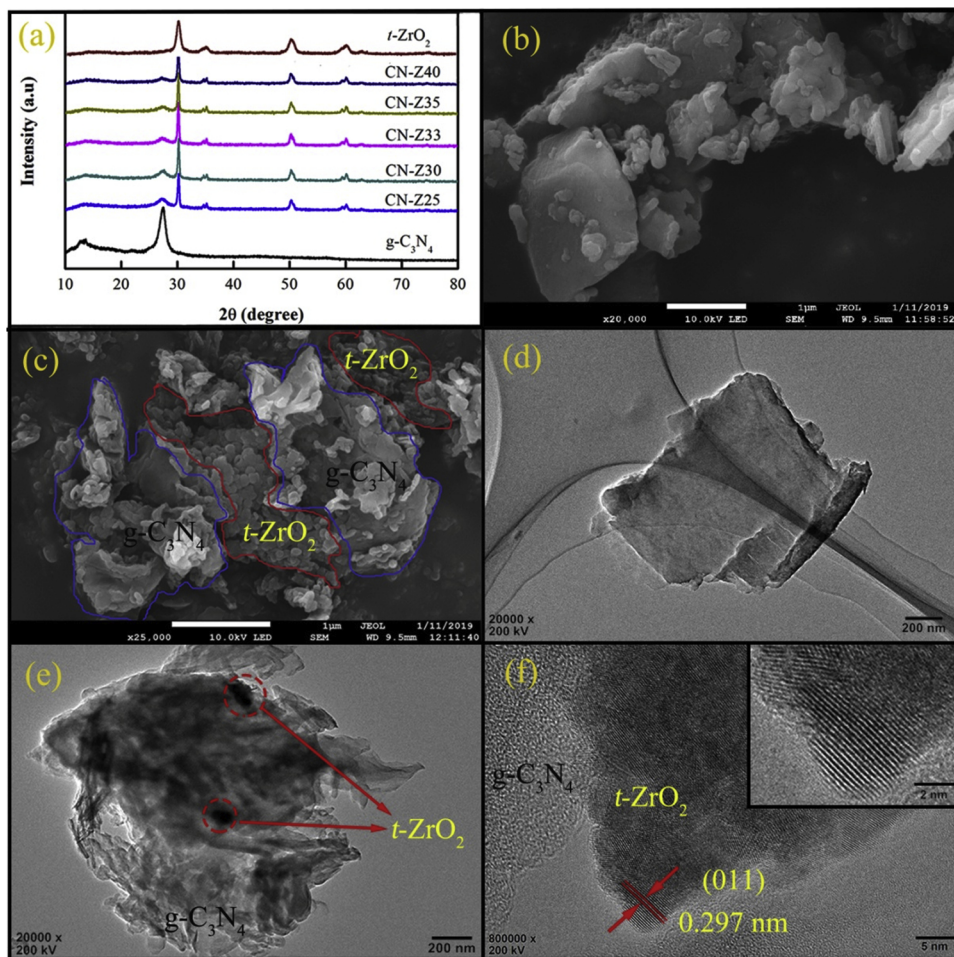
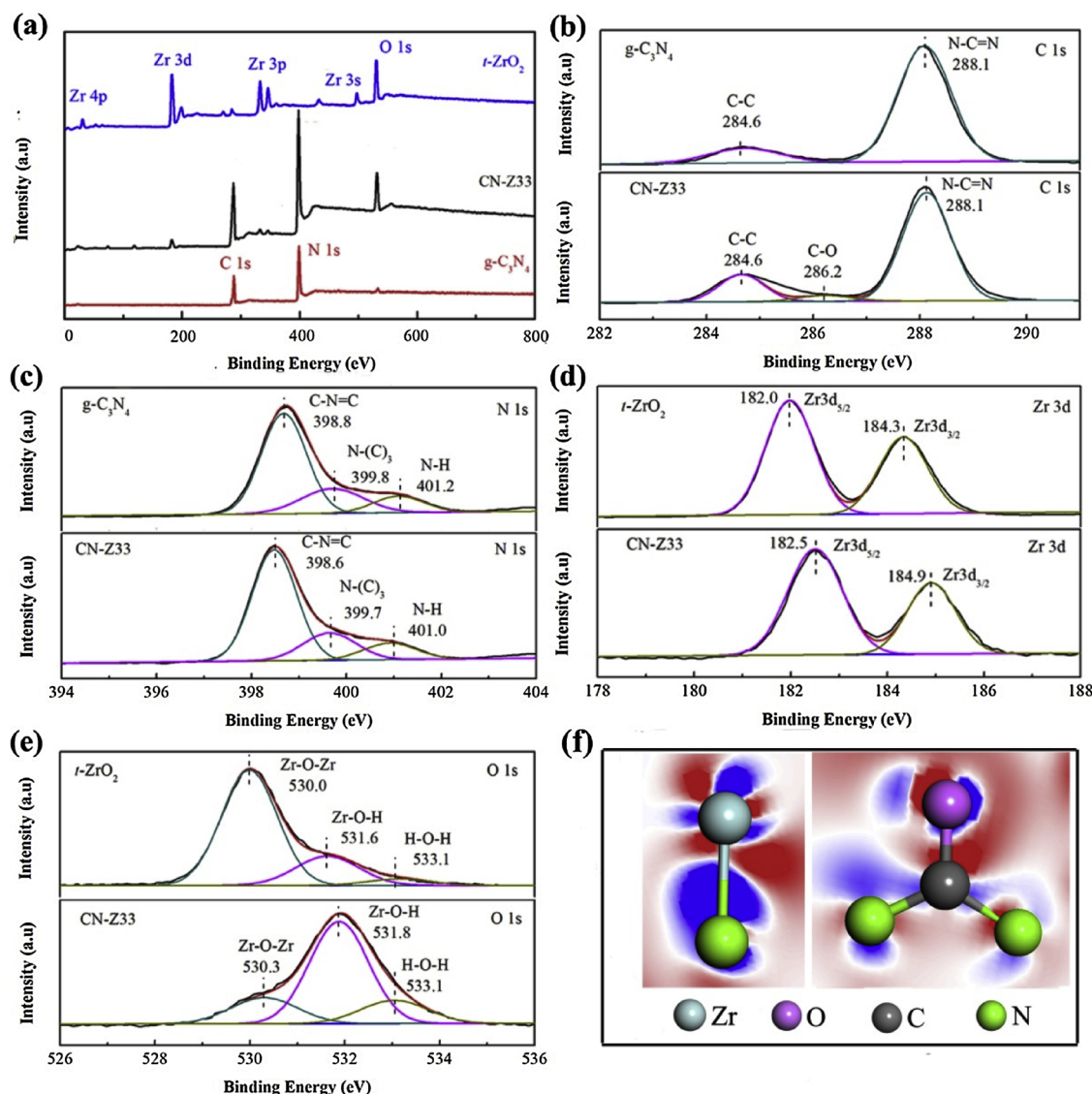


Fig. 2. (a) XRD patterns of all samples. SEM images of (b)  $\text{g-C}_3\text{N}_4$  and (c) CN-Z33. TEM images of (d)  $\text{g-C}_3\text{N}_4$  and (e) CN-Z33, (f) HRTEM image of CN-Z33.



**Fig. 3.** XPS spectra of (a) *t*-ZrO<sub>2</sub>, g-C<sub>3</sub>N<sub>4</sub> and CN-Z33 samples. The (b) C 1s, (c) N 1s, (d) Zr 3d and (e) O 1s diffraction peaks of them. The electronic density difference of (f) Zr–N and O–C–N bonds in *t*-ZrO<sub>2</sub>/g-C<sub>3</sub>N<sub>4</sub> system, where red and green regions denote the electron loss and accumulation, respectively. (For interpretation of the references to colour in this figure legend, the reader is referred to the web version of this article).

(cycloid dotted lines, 50–80 nm) supporting on the ultrathin g-C<sub>3</sub>N<sub>4</sub> film (around 800 nm). The HRTEM image of CN-Z33 sample (Fig. 2f) shows the details of the interfaces between *t*-ZrO<sub>2</sub> and g-C<sub>3</sub>N<sub>4</sub> phases, where the ordered and disordered atomic arrangement denote the crystalline *t*-ZrO<sub>2</sub> and organic g-C<sub>3</sub>N<sub>4</sub> phases, respectively. The interplanar spacing of 0.297 nm in *t*-ZrO<sub>2</sub> phase is assigned to the (011) planes [42]. Based on the morphologies of samples, the structural models of g-C<sub>3</sub>N<sub>4</sub> film (Fig. S1a) and *t*-ZrO<sub>2</sub>/g-C<sub>3</sub>N<sub>4</sub> (*t*-ZrO<sub>2</sub> phase is supported on g-C<sub>3</sub>N<sub>4</sub> film, Fig. S1b) were built for the density functional theory (DFT) simulations, where the oxygen dopants are considered to replace the N atoms of g-C<sub>3</sub>N<sub>4</sub> film in *t*-ZrO<sub>2</sub>/g-C<sub>3</sub>N<sub>4</sub> system [43] (see the Supporting Information for all simulation details).

The surface electronic states of *t*-ZrO<sub>2</sub>, g-C<sub>3</sub>N<sub>4</sub> and CN-Z33 samples were ascertained by X-ray photoelectron spectroscopy (XPS) measurement. As shown in Fig. 3a, the diffraction peaks represent the C and N elements in pristine g-C<sub>3</sub>N<sub>4</sub> sample and the Zr and O elements in pristine *t*-ZrO<sub>2</sub> sample (the weak C 1s peak originating from carbon substrate). Meanwhile, the CN-Z33 sample consist of C, N, Zr and O elements and thus contain both g-C<sub>3</sub>N<sub>4</sub> and *t*-ZrO<sub>2</sub> phases. Moreover, the diffraction peaks of all elements are compared each other to analyze the changes of electronic states. In Fig. 3b, the C 1s diffraction peaks at

284.6 and 288.1 eV denote the electronic states of graphite-like *sp*<sup>2</sup> (C–C) and *sp*<sup>3</sup> (N–C≡N) [44], which are present in both g-C<sub>3</sub>N<sub>4</sub> and CN-Z33 samples. The peak at 286.2 eV of CN-Z33 sample denotes a small amount of C–O bonding in the interface of *t*-ZrO<sub>2</sub>/g-C<sub>3</sub>N<sub>4</sub> [33]. In Fig. 3c, three N 1s diffraction peaks at 398.8, 399.8, and 401.2 eV of g-C<sub>3</sub>N<sub>4</sub> sample denote the C≡N=C, N–(C)<sub>3</sub> and N–H bonding, respectively [45–47]. In comparison to g-C<sub>3</sub>N<sub>4</sub> sample, the three peaks of CN-Z33 sample left-shift 0.1–0.2 eV, which indicates that the N atoms of g-C<sub>3</sub>N<sub>4</sub> phase acquire a certain amount of electrons from *t*-ZrO<sub>2</sub> phase. For *t*-ZrO<sub>2</sub> phase, the Zr 3d<sub>5/2</sub> and 3d<sub>3/2</sub> diffraction peaks locate at 182.0 and 184.3 eV for *t*-ZrO<sub>2</sub> sample [42,48] and right-shift 0.5–0.6 eV for CN-Z33 sample (see Fig. 3d), meanwhile, three O 1s diffraction peaks, denoting the Zr–O–Zr and Zr–O–H bonding [49,50], locate at 530.0 and 531.6 eV for *t*-ZrO<sub>2</sub> sample and also right-shift 0.2–0.3 eV for CN-Z33 sample (see Fig. 3e). The right-shifted diffraction peaks of Zr and O elements indicate the electrons transfer from Zr and O atoms to the N atoms of g-C<sub>3</sub>N<sub>4</sub> phase, which is consistent with the calculated electronic density differences of *t*-ZrO<sub>2</sub>/g-C<sub>3</sub>N<sub>4</sub> system by DFT simulation. Fig. 3f shows the electron transformation from *t*-ZrO<sub>2</sub> to oxygen doped g-C<sub>3</sub>N<sub>4</sub> since the conduction band minimum (CBM) level of g-C<sub>3</sub>N<sub>4</sub> film is lower than that of *t*-ZrO<sub>2</sub>

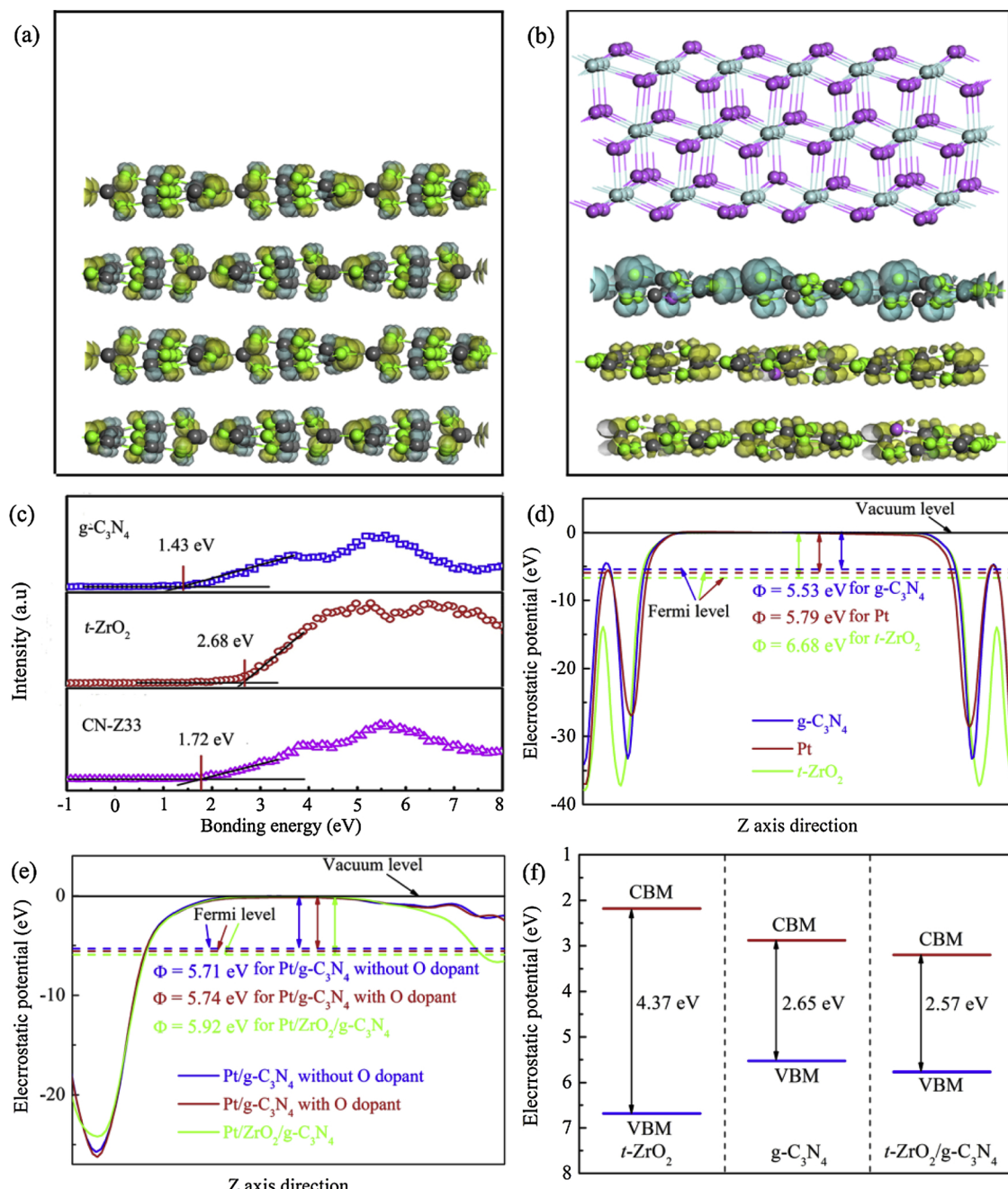


**Fig. 4.** The orbitals of VBM (blue) and CBM (yellow) of (a)  $g\text{-C}_3\text{N}_4$  film and (b)  $t\text{-ZrO}_2/g\text{-C}_3\text{N}_4$  interface. (c) The experimental XPS valence band spectra of  $t\text{-ZrO}_2$ ,  $g\text{-C}_3\text{N}_4$  and  $t\text{-ZrO}_2/g\text{-C}_3\text{N}_4$  samples. Average potential profile along Z axis direction of (d) pristine  $t\text{-ZrO}_2$ , Pt,  $g\text{-C}_3\text{N}_4$  systems, (e) Pt/g-C<sub>3</sub>N<sub>4</sub> with and without O dopant and Pt/t-ZrO<sub>2</sub>/g-C<sub>3</sub>N<sub>4</sub> systems. (f) The schematic band structures of  $t\text{-ZrO}_2$ ,  $g\text{-C}_3\text{N}_4$  and interface of  $t\text{-ZrO}_2/g\text{-C}_3\text{N}_4$  systems. (For interpretation of the references to colour in this figure legend, the reader is referred to the web version of this article).

nanoparticle (see Fig. 4f) and thus the transferred electrons prior to occupy the empty orbital of  $g\text{-C}_3\text{N}_4$  phase with low level, where the red and blue regions denote the electron loss and accumulation, respectively. Noted that the CBM and valence band maximum (VBM) levels of  $t\text{-ZrO}_2$  and  $g\text{-C}_3\text{N}_4$  systems are estimated by the calculated work function (see Fig. 4d) and experimental optical absorption curve (see Fig. 7a). The order of the VBM in  $t\text{-ZrO}_2$ ,  $g\text{-C}_3\text{N}_4$  and  $t\text{-ZrO}_2/g\text{-C}_3\text{N}_4$  is consistent with the experimental results of XPS valence band spectra, as shown in Fig. 4c. In addition, the Zr–O–H bonding comes from the adsorption of water molecule on  $t\text{-ZrO}_2$  surface, and the O 1s diffraction peak at 533.1 eV denotes the H–O–H bonding in water molecule, the CN-Z33 sample has thus better hydrophilicity than  $t\text{-ZrO}_2$  sample due to the higher intensity of Zr–O–H and H–O–H peaks in CN-Z33 sample.

Photocatalytic efficiency of all samples were measured by splitting water for hydrogen generation under visible-light ( $\lambda > 420$  nm). As shown in Fig. 5a, the amount of hydrogen generations are 0.000, 9.030, 16.038, 26.533, 36.125, 21.243 and 13.588  $\mu\text{mol h}^{-1}$  for Pt/t-ZrO<sub>2</sub>, Pt/g-C<sub>3</sub>N<sub>4</sub>, Pt/CN-Z25, Pt/CN-Z30, Pt/CN-Z33, Pt/CN-Z35 and Pt/CN-Z40 samples, respectively. Thereinto, the Pt/CN-Z33 sample has the highest hydrogen generation which is quadruple that of Pt/g-C<sub>3</sub>N<sub>4</sub> sample. Meanwhile, the hydrogen generation of Pt/CN-Z33 sample is compared with other experimental data in Table S1, and our Pt/CN-Z33 sample has higher efficiency of hydrogen generation than the others. Moreover, the Pt/CN-Z33 sample still has high catalytic efficiency after three cycles (30.695  $\mu\text{mol h}^{-1}$ ), suggesting a good catalytic stability. Moreover, the solar-to-hydrogen (STH) energy conversion

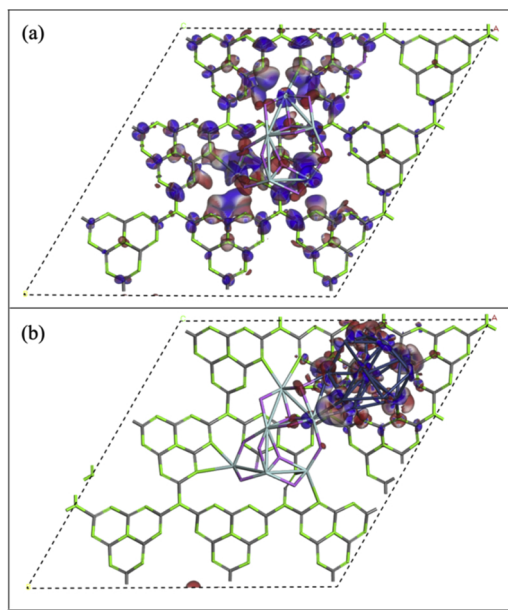


Fig. 5. The electronic redistributions of (a)  $g\text{-C}_3\text{N}_4$  layer after supporting  $t\text{-ZrO}_2$  cluster and (b)  $t\text{-ZrO}_2/g\text{-C}_3\text{N}_4$  after supporting Pt cluster.

efficiency was calculated from the following equation [51]:

$$STH = R \times \Delta G_r / (P_{\text{sun}} \times S) \quad (1)$$

where  $R$ ,  $\Delta G_r$ ,  $P_{\text{sun}}$  and  $S$  denote the rate of  $\text{H}_2$  evolution during the water splitting reaction, the Gibbs energy for the water splitting reaction (237.13 kJ/mol), the average energy flux of sunlight (55.9 mWcm<sup>-2</sup>, calculation method following ref. [52,53]), and the irradiated photocatalyst area (cylindrical reaction vessel with the area of 19.625 cm<sup>2</sup>), respectively. The STH of our Pt/CN-Z33 sample was calculated to be 0.215%, which is larger than the conventional efficiency of 0.1%.

### 3. Discussion

Optical and photoelectric measurements of our samples were performed to investigate the enhancement mechanisms of photocatalytic performances. Fig. 6a shows the UV-vis diffuse reflectance spectra of them. The absorption edges are 460 nm for  $g\text{-C}_3\text{N}_4$  sample but only 275 nm for  $t\text{-ZrO}_2$  sample. As results,  $g\text{-C}_3\text{N}_4$  sample can be responded by UV light and part of visible-light but  $t\text{-ZrO}_2$  sample is only responsive for UV light. For all the composite samples, the absorption edges red-shift 5–30 nm in comparison to that of  $g\text{-C}_3\text{N}_4$  sample, it

indicates that composite samples have larger visible-light absorption capacity than  $g\text{-C}_3\text{N}_4$  sample, which may be caused by the introduced oxygen atom in  $g\text{-C}_3\text{N}_4$  film during sintering process [43]. Thereinto, the CN-Z33 sample with absorption edge of 490 nm displays the largest absorption capacity among our samples. Based on Kubelk-Munk method, the optical forbidden gaps ( $E_g$ ) are 4.37, 2.65, and 2.57 eV for the  $t\text{-ZrO}_2$ ,  $g\text{-C}_3\text{N}_4$  and ZCN3 samples, respectively.

The photoluminescence (PL), transient state photoluminescence (TSPL), electrochemical impedance spectra (EIS), and transient photocurrent were measured to obtain the photoelectric performances of samples. The PL and TSPL reflects the photogenerated carrier recombination probability, as shown in Fig. 7b and c. The composite samples have lower PL intensities and longer fluorescence lifetime, and thus longer photogenerated carrier lifetime than  $g\text{-C}_3\text{N}_4$  and  $t\text{-ZrO}_2$  samples at an excitation wavelength of 325 nm, which consists with the DFT simulation. Unlike pristine  $g\text{-C}_3\text{N}_4$  film, whose orbitals of VBM and CBM locate at the neighboring C and N atoms of every atomic layer [16,54–56], as shown in Fig. 4a, the orbitals of VBM and CBM in  $t\text{-ZrO}_2/g\text{-C}_3\text{N}_4$  composite locate at the nearest atomic layer and the other atomic layers of  $g\text{-C}_3\text{N}_4$  film, respectively (see Fig. 4b). The significant separation of VBM and CBM in space can effectively suppress the recombination of photogenerated electron/hole pairs in  $t\text{-ZrO}_2/g\text{-C}_3\text{N}_4$  composite, which attributes to the electron redistribution of  $g\text{-C}_3\text{N}_4$  monolayer after supporting  $t\text{-ZrO}_2$  nanoparticle (see Fig. 5a), it is worth noting that the electron redistribution of  $g\text{-C}_3\text{N}_4$  monolayer is basically unchanged (see Fig. 5b). In here, the CN-Z33 sample with the lowest PL intensity and the longest fluorescence lifetime should have the longest photogenerated carrier lifetime. Moreover, the EIS reflects the electron transfer resistances of all samples, as shown in Fig. 7d. All composite samples display smaller arc radius and thus smaller electron transfer resistances than  $g\text{-C}_3\text{N}_4$  and  $t\text{-ZrO}_2$  samples where the CN-Z33 sample has the smallest arc radius and smallest electron transfer resistances. Meanwhile, Fig. 7e shows that the CN-Z33 sample has the highest transient photocurrent response and carrier transferability. In brief, the  $t\text{-ZrO}_2$  nanoparticle could effectively improve the photogenerated carrier lifetime and transferability of  $g\text{-C}_3\text{N}_4$  film, the improved photoelectric and photocatalytic performances of  $g\text{-C}_3\text{N}_4$  film are mainly attributed to the electronic redistribution after supporting  $t\text{-ZrO}_2$  nanoparticles.

Since the hydrogen production depends on the hydrogen adsorption free energy ( $\Delta G_H$ , calculated by Eq. S2) and reaction energy barriers during the HER processes, the corresponding DFT simulations were calculated to demonstrate the increase of reaction efficiency, where the  $g\text{-C}_3\text{N}_4$  monolayer was considered since the HER generally occurs on supporting Pt cluster. To verify the adsorption site of Pt atoms on substrates, the bonding energies of the first Pt atom on the different sites of pristine  $g\text{-C}_3\text{N}_4$  (Fig. 8a), O doped  $g\text{-C}_3\text{N}_4$  (Fig. 8b) and  $t\text{-ZrO}_2/g\text{-C}_3\text{N}_4$  (Fig. 8c) systems were calculated by Eq. S1. Results show that

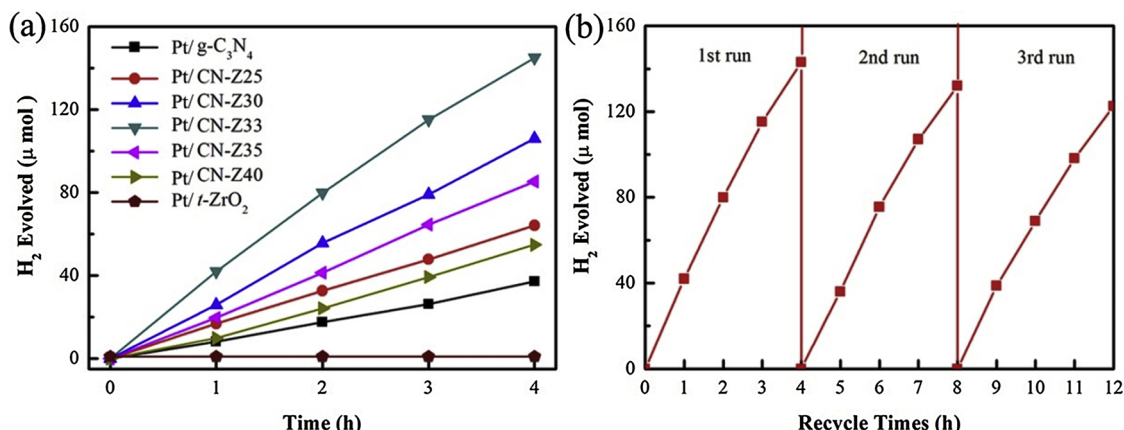
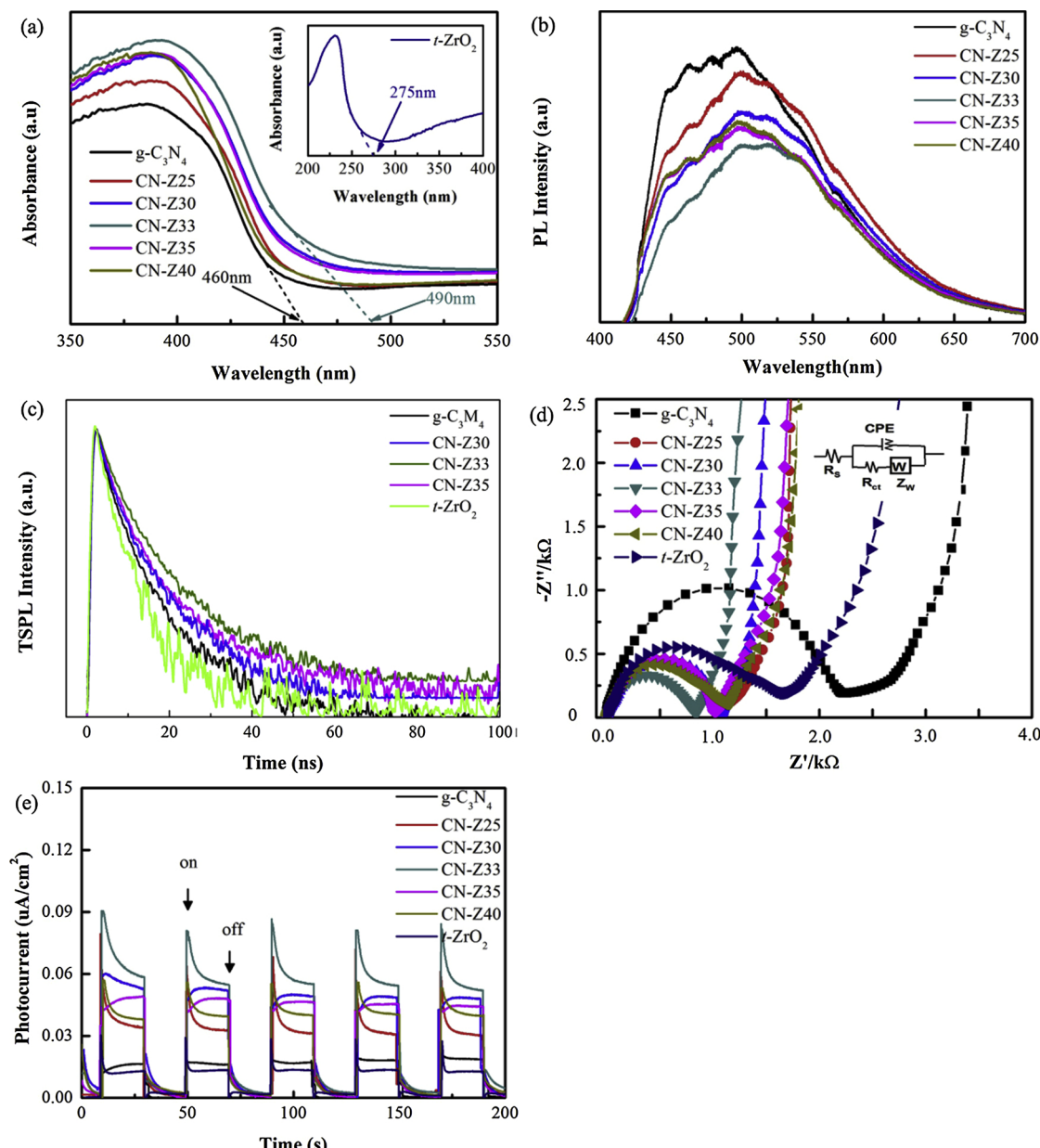


Fig. 6. (a) Photocatalytic  $\text{H}_2$  evolution by all samples under visible-light ( $\lambda > 420 \text{ nm}$ ); (b) Recycle runs of  $\text{H}_2$  evolution by CN-Z33 sample.



**Fig. 7.** (a) UV–vis diffuse reflection spectra, (b) PL emission spectra, (c) electrochemical impedance spectra and (d) transient photocurrent response of prepared samples.

the Pt atom priors to be attached to the sites 1 and 2 of  $t\text{-ZrO}_2/g\text{-C}_3\text{N}_4$ , and thus the Pt cluster priors to load on the surface of  $g\text{-C}_3\text{N}_4$  film against the  $t\text{-ZrO}_2$  cluster (see Fig. S2a). Moreover, the electronic structure of all systems were calculated. The calculation results show that the work function of  $g\text{-C}_3\text{N}_4$  monolayer are slightly increased by the oxygen dopants, and the work function of  $\text{Pt}/t\text{-ZrO}_2/g\text{-C}_3\text{N}_4$  is larger than that of  $\text{Pt}/g\text{-C}_3\text{N}_4$  with and without oxygen dopant on account of the large work function of  $t\text{-ZrO}_2$  cluster (see Fig. 4e). This implies that  $\text{Pt}/g\text{-C}_3\text{N}_4$  sample has a higher valence electron level and thus a stronger interaction with H atom. After supporting  $t\text{-ZrO}_2$  nanoparticle, the  $\text{Pt}/t\text{-ZrO}_2/g\text{-C}_3\text{N}_4$  composite has a lower valence electron level, leading to the weaker  $\Delta G_{\text{H}}$ . This issue is verified by the calculated Gibbs free energy diagram and the corresponding  $\Delta G_{\text{H}}$  values for HER, as shown in Fig. 7a. It is evident that, the  $\Delta G_{\text{H}}$  value of  $\text{Pt}/t\text{-ZrO}_2/g\text{-C}_3\text{N}_4$  system ( $-0.15\text{ eV}$ ) is weaker than that of  $\text{Pt}/g\text{-C}_3\text{N}_4$  systems ( $-0.27\text{ eV}$  and  $-0.29\text{ eV}$  for  $g\text{-C}_3\text{N}_4$  with and without oxygen dopant), and the  $\Delta G_{\text{H}}$  value of  $\text{Pt}/t\text{-ZrO}_2/g\text{-C}_3\text{N}_4$  system is closer to zero in comparison to that of  $\text{Pt}/g\text{-C}_3\text{N}_4$  systems (see Fig. 8e), which

indicates that the supporting  $t\text{-ZrO}_2$  nanoparticles can effectively reduce the free energy barrier of HER and improve the intrinsic catalytic efficiency of  $\text{Pt}/g\text{-C}_3\text{N}_4$ .

To clarify the reaction mechanism of the HER on Pt cluster of  $\text{Pt}/g\text{-C}_3\text{N}_4$  and  $\text{Pt}/t\text{-ZrO}_2/g\text{-C}_3\text{N}_4$  composites, three reaction paths of Volmer, Heyrovsky, and Tafel reactions have been conducted by DFT simulation, as shown in Fig. 8, including the initial state (IS), transition state (TS), and final state (FS). Note that two  $\text{H}_2\text{O}$  groups with one  $\text{H}^+$  [ $(\text{H}_5\text{O}_2)^+$ ] were utilized as the proton in solution [57,58], and the atomic structures of all IS, TS and FS are presented in Figs. S2–S4. For the hydrogen adsorption process, the energy barrier values of Volmer reaction are  $0.28\text{ eV}$  for  $\text{Pt}/t\text{-ZrO}_2/g\text{-C}_3\text{N}_4$  composite, but  $0.36\text{ eV}$  and  $0.34\text{ eV}$  for  $\text{Pt}/g\text{-C}_3\text{N}_4$  with and without oxygen dopant, respectively (see Fig. 9a). For the dehydrogenation processes, the energy barrier values of Heyrovsky (Tafel) reaction are  $0.42$  ( $0.71$ )  $\text{eV}$  for  $\text{Pt}/t\text{-ZrO}_2/g\text{-C}_3\text{N}_4$  composite, but  $0.74$  ( $1.09$ )  $\text{eV}$  and  $0.70$  ( $0.99$ )  $\text{eV}$  for  $\text{Pt}/g\text{-C}_3\text{N}_4$  with and without oxygen dopant, respectively (see Fig. 9b and c). On account of the smaller energy barrier value, the Heyrovsky reaction is

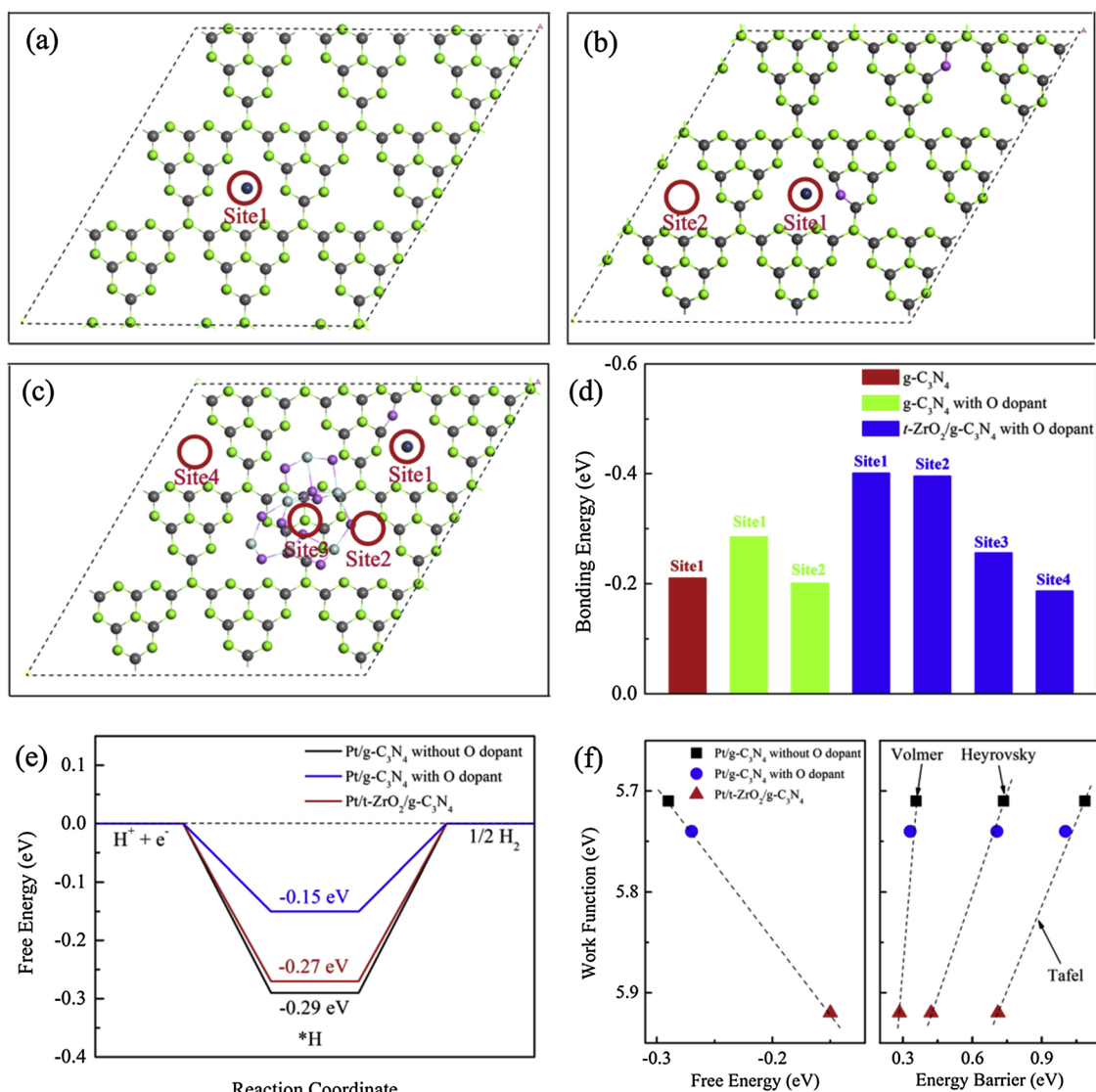


**Fig. 8.** The structures of Pt atom on (a) pristine  $\text{g-C}_3\text{N}_4$ , (b)  $\text{g-C}_3\text{N}_4$  with O dopant and (c)  $\text{t-ZrO}_2/\text{g-C}_3\text{N}_4$  with O dopant, the gray, green, pink and dark blue balls denote the C, N, O and Pt atoms, respectively; (d) the bonding energy values of Pt atom on substrates, calculated by Eq. (e) Free energy diagram for hydrogen evolution at equilibrium ( $T = 300 \text{ K}$  and potential  $U = 0 \text{ V}$ ); (f) the relationships between the work function and the adsorption free energy, energy barriers for Volmer, Heyrovsky and Tafel reactions of  $\text{Pt}/\text{t-ZrO}_2/\text{g-C}_3\text{N}_4$  and  $\text{Pt}/\text{g-C}_3\text{N}_4$  with and without O dopant. (For interpretation of the references to colour in this figure legend, the reader is referred to the web version of this article).

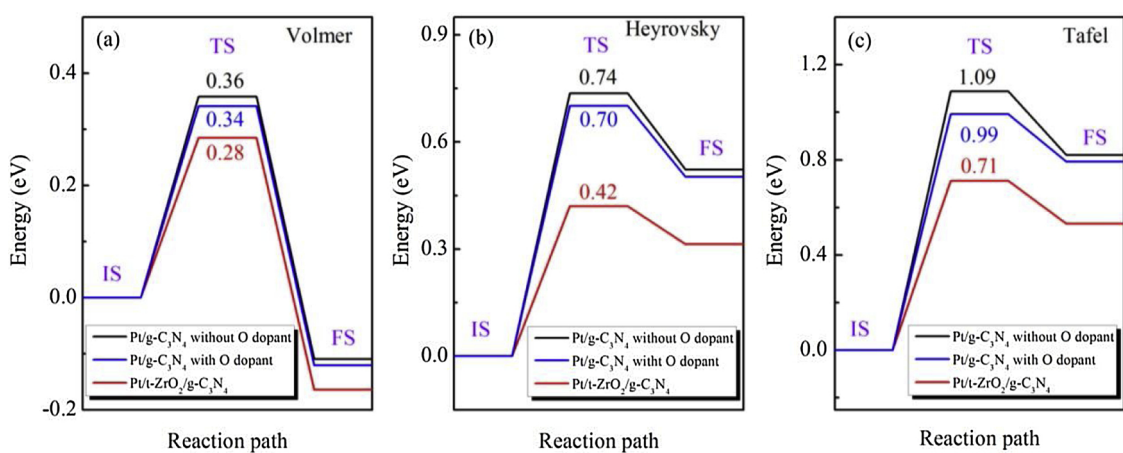


**Fig. 9.** Reaction paths of (a) Volmer, (b) Heyrovsky, and (c) Tafel reactions of the HER on  $\text{Pt}/\text{g-C}_3\text{N}_4$  with and without O dopant and  $\text{Pt}/\text{t-ZrO}_2/\text{g-C}_3\text{N}_4$  systems.

preferable in comparison to the Tafel reaction for Pt/g-C<sub>3</sub>N<sub>4</sub> and Pt/t-ZrO<sub>2</sub>/g-C<sub>3</sub>N<sub>4</sub> systems, and thus the HER on them should follow a Volmer–Heyrovsky mechanism with the rate-determining step of Heyrovsky reaction. Moreover, the Pt/t-ZrO<sub>2</sub>/g-C<sub>3</sub>N<sub>4</sub> system should have a faster reaction rate than Pt/g-C<sub>3</sub>N<sub>4</sub> with and without oxygen dopant systems since the reaction energy barriers of both Volmer and Heyrovsky reactions on Pt/t-ZrO<sub>2</sub>/g-C<sub>3</sub>N<sub>4</sub> system are lower than the corresponding reactions on Pt/g-C<sub>3</sub>N<sub>4</sub> systems. The lower energy barriers of Volmer and Heyrovsky reactions also depend on the lower VBM level or larger work function of Pt/t-ZrO<sub>2</sub>/g-C<sub>3</sub>N<sub>4</sub> in comparison to that of Pt/g-C<sub>3</sub>N<sub>4</sub> (Fig. 8f).

In light of the above results, a new Pt/t-ZrO<sub>2</sub>/g-C<sub>3</sub>N<sub>4</sub> as a composite photocatalyst is designed and its enhancement mechanisms of photocatalytic performances at the electronic and energetic levels are studied.

#### 4. Conclusion

In summary, a novel Pt/t-ZrO<sub>2</sub>/g-C<sub>3</sub>N<sub>4</sub> photocatalyst has been designed and analyzed with the aid of experimental measurements and DFT simulations. By supporting the t-ZrO<sub>2</sub> nanoparticle, the Pt/t-ZrO<sub>2</sub>/g-C<sub>3</sub>N<sub>4</sub> composite has an evident improvement of the photogenerated carrier lifetime and transferability due to the electronic redistribution, and a reduction of the reaction energy barriers thanks to the enlargement of work function. The photocatalyst of Pt/CN-Z33 exhibits excellent HER catalytic performances with hydrogen generation of 722.5 μmol(gh)<sup>-1</sup>, STH energy conversion efficiency of 0.215% and good catalytic stability. The modification strategy proposed can also be extended to the design of other high-efficiency catalysts by selecting semiconductors with suitable work functions.

#### Acknowledgements

This work was supported in part by the Natural Science Foundation of Zhejiang Province, China (LY18E020007, LQ18E030005 and LY19F020006). Computational resources were provided by the Jilin University.

#### Appendix A. Supplementary data

Supplementary material related to this article can be found, in the online version, at doi:<https://doi.org/10.1016/j.apcatb.2019.03.079>.

#### References

- [1] X. Wang, K. Maeda, A. Thomas, K. Takanabe, G. Xin, J.M. Carlsson, K. Domen, M. Antonietti, *Nat. Mater.* 8 (2009) 76–80.
- [2] M. Wen, K. Mori, T. Kamegawa, H. Yamashita, *Chem. Commun.* 50 (2014) 11645–11648.
- [3] X. Chen, L. Liu, P.Y. Yu, S.S. Mao, *Science* 331 (2011) 746–750.
- [4] A. Fujishima, K. Honda, *Nature* 238 (1972) 37–38.
- [5] Y. Wang, S. Zhao, Y. Wang, D.A. Laleyan, Y. Wu, B. Ouyang, P. Ou, J. Song, Z. Mi, *Nano Energy* 51 (2018) 54–60.
- [6] Z.F. Huang, J. Song, K. Li, M. Tahir, Y.T. Wang, L. Pan, L. Wang, X. Zhang, J.J. Zou, *J. Am. Chem. Soc.* 138 (2016) 1359–1365.
- [7] S.M. Sun, X.M. Li, W.Z. Wang, L. Zhang, X. Sun, *Appl. Catal. B: Environ.* 200 (2017) 323–329.
- [8] H. Xu, J. Yi, X. She, Q. Liu, L. Song, S. Chen, Y. Yang, Y. Song, R. Vajtai, J. Lou, H. Li, S. Yuan, J. Wu, P.M. Ajayan, *Appl. Catal. B: Environ.* 220 (2018) 379–385.
- [9] J. Gu, J.A. Aguiar, S. Ferrere, K.X. Steirer, Y. Yan, C. Xiao, James L. Young, M. Al-Jassim, N.R. Neale, J.A. Turner, *Nat. Energy* 2 (2017) 16192.
- [10] S.S.K. Ma, T. Hisatomi, K. Maeda, Y. Moriya, K. Domen, *J. Am. Chem. Soc.* 134 (2012) 19993–19996.
- [11] Y. Moriya, T. Takata, K. Domen, *Coord. Chem. Rev.* 257 (2013) 1957–1969.
- [12] Z.L. Guo, J. Zhou, L.G. Zhu, Z.M. Sun, *J. Mater. Chem. A* 4 (2016) 11446–11452.
- [13] V.M.H. Ng, H. Huang, K. Zhou, P.S. Lee, W. Que, J.Z. Xu, L.B. Kong, *J. Mater. Chem. A* 5 (2017) 3039–3068.
- [14] C. Yang, W. Huang, L.C. da Silva, K.A.I. Zhang, X. Wang, *Chem.-Eur. J.* 24 (2018) 17454–17458.
- [15] H. Ou, X. Chen, L. Lin, Y. Fang, X. Wang, *Angew. Chem. Int. Ed. Engl.* 57 (2018) 8729–8733.
- [16] S. Lu, Z.W. Chen, C. Li, H.H. Li, Y.F. Zhao, Y.Y. Gong, L.Y. Niu, X.J. Liu, T. Wang, C.Q. Sun, *J. Mater. Chem. A* 4 (2016) 14827–14838.
- [17] S.-S. Yi, X.-B. Zhang, B.-R. Wulan, J.-M. Yan, Q. Jiang, *Energy Environ. Sci.* 11 (2018) 3128–3156.
- [18] Y.Y. Gong, Y.J. Wu, Y. Xu, L. Li, C. Li, X.J. Liu, L.Y. Niu, *Chem. Eng. J.* 350 (2018) 257–267.
- [19] J.J. Yi, X.J. She, Y.H. Song, M. Mao, K.X. Xia, Y.G. Xu, Z. Mo, J.J. Wu, H. Xu, H.M. Li, *Chem. Eng. J.* 335 (2018) 282–289.
- [20] J.J. Yi, H.P. Li, Y.J. Gong, X.J. She, Y.H. Song, Y.G. Xu, J.J. Deng, S.Q. Yuan, H. Xu, H.M. Li, *Appl. Catal. B: Environ.* 243 (2019) 330–336.
- [21] T.R. Gordon, M. Cargnello, T. Paik, F. Mangolini, R.T. Weber, P. Fornasiero, C.B. Murray, *J. Am. Chem. Soc.* 134 (2012) 6751–6761.
- [22] Y.P. Zhu, T.Z. Ren, Z.Y. Yuan, *ACS Appl. Mater. Interface* 7 (2015) 16850–16856.
- [23] J. Wang, L. Tang, G. Zeng, Y. Deng, H. Dong, Y. Liu, L. Wang, B. Peng, C. Zhang, F. Chen, *Appl. Catal. B: Environ.* 222 (2018) 115–123.
- [24] J. Low, B. Cheng, J. Yu, *Appl. Surf. Sci.* 392 (2017) 658–686.
- [25] T. Kamegawa, D. Yamahana, H. Yamashita, *J. Phys. Chem. C* 114 (2010) 15049–15053.
- [26] B.B. Liu, X.J. Liu, J.Y. Liu, C.J. Feng, Z. Li, C. Li, Y.Y. Gong, L.K. Pan, S.Q. Xu, C.Q. Sun, *Appl. Catal. B: Environ.* 226 (2018) 234–241.
- [27] G. Li, X. Nie, J. Chen, Q. Jiang, T. An, P.K. Wong, H. Zhang, H. Zhao, H. Yamashita, *Water Res.* 86 (2015) 17–24.
- [28] L. Renuka, K.S. Anantharaju, Y.S. Vidya, H.P. Nagaswarupa, S.C. Prashantha, S.C. Sharma, H. Nagabhushana, G.P. Darshan, *Appl. Catal. B: Environ.* 210 (2017) 97–115.
- [29] D.L. Jiang, J. Li, C.S. Xing, Z.Y. Zhang, S.C. Meng, M. Chen, *ACS Appl. Mater. Interface* 7 (2015) 19234–19242.
- [30] J. Ran, W. Guo, H. Wang, B. Zhu, J. Yu, S.Z. Qiao, *Adv. Mater.* 30 (2018) e1800128.
- [31] T. Muhammed, M. Xia, W. Lei, F. Wang, *Appl. Catal. B: Environ.* 238 (2018) 568–575.
- [32] B. Lin, H. Li, H. An, W.B. Hao, J.J. Wei, Y.Z. Dai, C.S. Ma, G.D. Yang, *Appl. Catal. B: Environ.* 220 (2018) 542–552.
- [33] S.Q. Zhao, Z.Y. Tang, S.J. Guo, M.M. Han, C. Zhu, Y.J. Zhou, L. Bai, J. Gao, H. Huang, Y.Y. Li, Y. Liu, Z.H. Kang, *ACS Catal.* 8 (2018) 188–197.
- [34] L. Zhang, X.L. Fu, S.G. Meng, X.L. Jiang, J.H. Wang, S.F. Chen, *J. Mater. Chem. A* 3 (2015) 23732–23742.
- [35] Y.G. Tan, Z. Shu, J. Zhou, T.T. Li, W.B. Wang, Z.L. Zhao, *Appl. Catal. B: Environ.* 230 (2018) 260–268.
- [36] Z. Mao, J. Chen, Y. Yang, D. Wang, L. Bie, B.D. Fahlman, *ACS Appl. Mater. Interface* 9 (2017) 12427–12435.
- [37] K. Xu, J. Feng, *RSC Adv.* 7 (2017) 45369–45376.
- [38] I. Ud Din, M.S. Shaharun, D. Subbarao, A. Naeem, *J. Power Sources* 274 (2015) 619–628.
- [39] J.Q. Zhang, L. Li, Z.X. Xiao, D. Liu, S. Wang, J.J. Zhang, Y.T. Hao, W.Z. Zhang, *ACS Sustain. Chem. Eng.* 4 (2016) 2037–2046.
- [40] J. Liu, T. Zhang, Z. Wang, G. Dawson, W. Chen, *J. Mater. Chem.* 21 (2011) 14398–14401.
- [41] J.J. Xue, S.S. Ma, Y.M. Zhou, Z.W. Zhang, M. He, *ACS Appl. Mater. Interface* 7 (2015) 9630–9637.
- [42] H. Xie, J. Lu, M. Shekhar, J.W. Elam, W.N. Delgass, F.H. Ribeiro, E. Weitz, K.R. Poepelmeier, *ACS Catal.* 3 (2013) 61–73.
- [43] S. Lu, C. Li, H.H. Li, Y.F. Zhao, Y.Y. Gong, L.Y. Niu, X.J. Liu, T. Wang, *Appl. Surf. Sci.* 392 (2017) 966–974.
- [44] X.Y. Li, Y.H. Pi, L.Q. Wu, Q.B. Xia, J.L. Wu, Z. Li, J. Xiao, *Appl. Catal. B: Environ.* 202 (2017) 653–663.
- [45] H.J. Li, D.J. Qian, M. Chen, *ACS Appl. Mater. Interface* 7 (2015) 25162–25170.
- [46] H.-B. Fang, X.-H. Zhang, J. Wu, N. Li, Y.-Z. Zheng, X. Tao, *Appl. Catal. B: Environ.* 225 (2018) 397–405.
- [47] S.-S. Yi, J.-M. Yan, B.-R. Wulan, S.-J. Li, K.-H. Liu, Q. Jiang, *Appl. Catal. B: Environ.* 200 (2017) 477–483.
- [48] X. Chen, Y.T. Liu, X.N. Xia, L.L. Wang, *Appl. Surf. Sci.* 407 (2017) 470–478.
- [49] A.P. Gaikwad, C.A. Betty, D. Tyagi, R. Rao, A.K. Tripathi, R. Sasikala, *Mol. Catal.* 435 (2017) 128–134.
- [50] L. Song, X.B. Cao, L. Li, *ACS Appl. Mater. Interface* 10 (2018) 31249–31259.
- [51] Z. Wang, C. Li, K. Domen, *Chem. Soc. Rev.* (2019) 2109–2125, <https://doi.org/10.1039/C8CS00542G>.
- [52] Q. Wang, T. Hisatomi, Q. Jia, H. Tokudome, M. Zhong, C. Wang, Z. Pan, T. Takata, M. Nakabayashi, N. Shibata, Y. Li, I.D. Sharp, A. Kudo, T. Yamada, K. Domen, *Nat. Mater.* 15 (2016) 611–615.
- [53] K. Ma, O. Yehezkel, D.W. Domaille, H.H. Funke, J.N. Cha, *Angew. Chem. Int. Ed.* 54 (2015) 11490–11494.
- [54] S.W. Cao, J.G. Yu, *J. Phys. Chem. Lett.* 5 (2014) 2101–2107.
- [55] W.J. Ong, L.L. Tan, Y.H. Ng, S.T. Yong, S.P. Chai, *Chem. Rev.* 116 (2016) 7159–7329.
- [56] H.H. Li, Y. Wu, L. Li, Y.Y. Gong, L.Y. Niu, X.J. Liu, T. Wang, C.Q. Sun, C. Li, *Appl. Surf. Sci.* 457 (2018) 735–744.
- [57] G.P. Gao, Q. Sun, A.J. Du, *J. Phys. Chem. C* 120 (2016) 16761–16766.
- [58] L.X. Chen, Z.W. Chen, Y. Wang, C.C. Yang, Q. Jiang, *ACS Catal.* 8 (2018) 8107–8114.